PHOTONICS Research

High-speed 2D beam steering based on a thin-film lithium niobate optical phased array with a large field of view

Wenlei Li,[1] Xu Zhao,[2] Jianghao He,[1] Hao Yan,[1] Bingcheng Pan,[1] Zichen Guo,[2] Xiang'e Han,[2] Jingye Chen,[1,3] Daoxin Dai,[1] and Yaocheng Shi[1,*]

[1]State Key Laboratory for Modern Optical Instrumentation, Center for Optical and Electromagnetic Research, International Research Center for Advanced Photonics, Ningbo Research Institute, College of Optical Science and Engineering, Zhejiang University, China
[2]School of Physics, Xidian University, Xi'an 710071, China
[3]e-mail: jingyechen@zju.edu.cn
*Corresponding author: yaocheng@zju.edu.cn

Received 2 August 2023; revised 10 September 2023; accepted 10 September 2023; posted 12 September 2023 (Doc. ID 502439); published 26 October 2023

An on-chip optical phased array (OPA) is considered as a promising solution for next generation solid-state beam steering. However, most of the reported OPAs suffer from low operating bandwidths, making them limited in many applications. We propose and demonstrate a high-speed 2D scanning OPA based on thin-film lithium niobate phase modulators with traveling-wave electrodes. The measured modulation bandwidth is up to 2.5 GHz. Moreover, an aperiodic array combined with a slab grating antenna is also used to suppress the grating lobes of far-field beams, which enables a large field of view (FOV) as well as small beam width. A 16-channel OPA demonstrates an FOV of 50° × 8.6° and a beam width of 0.73° × 2.8° in the phase tuning direction and the wavelength scanning direction, respectively.

https://doi.org/10.1364/PRJ.502439

1. INTRODUCTION

As a novel all-solid-state beam steering technology, an optical phased array (OPA) features compact size, high reliability, fast speed, and low cost [1,2]. OPA is considered to be an effective technology for many applications, including light detection and ranging (LIDAR) [3], holographic projection [4], and free-space optical communication [5]. Thanks to the mature complementary metal oxide semiconductor (CMOS) process platform, many high-performance on-chip OPAs have been proposed and demonstrated [6–9], for example, aliasing-free 180° beam steering [10,11], less than 0.1° beam width [12], and more than 1000 array elements scale [3]. However, we can notice that most of the reported OPA chips are based on thermo-optic effects to realize phase modulation among the array elements, resulting in relatively low beam steering speeds and limiting their practical applications.

Many different modulation mechanisms and material platforms are used to enhance the operating bandwidth of on-chip OPAs. The free-carrier plasma dispersion effect can provide high-speed electro-optical (EO) modulators for silicon photonics. Several OPAs based on carrier injection or carrier depletion type modulators have been proposed and realized with operating bandwidths of hundreds of MHz [13,14]. Though EO silicon modulators have excellent integration and scalability, the carrier will introduce significant additional absorption loss that increases the light source burden and leads to degradation of the far-field distribution of the OPAs. EO polymers have relatively large electro-optic coefficients, enabling ultra-high bandwidth phase modulators. EO-polymer-based OPAs also have demonstrated operating rates of the order of MHz, but the stability of the polymers has yet to be proven [15]. More recently, high-speed and stable OPAs based on an indium phosphide (InP) platform have been demonstrated, which is CMOS incompatible and also has the issue of additional loss associated with modulation [16–18]. More importantly, we can also notice that almost all of these high-speed OPAs mentioned above have a bandwidth of less than GHz.

Among these EO material platforms, thin-film lithium niobate (TFLN) offers significant advantages such as a high Pockels effect, tight optical field confinement capability, and low propagation loss [19]. TFLN modulators have demonstrated pure phase modulation with CMOS-compatible drive voltages and ultra-high bandwidths [20–22]. In addition, the wide transparency window and high power threshold of TFLN offer great potential for broadening the optical band and operating distance of OPAs. Therefore, the TFLN platform has great potential for realizing high-performance OPA chips. Although some TFLN OPAs have been reported previously [23–25], the scanning range and operating bandwidth are still

small, due to the antenna arrangement and RC-limited electrode design.

In this paper, we propose and demonstrate a TFLN-based 16-channel OPA with high speed and a large field of view (FOV). A traveling-wave modulator array is used to achieve high-speed pure-phase modulation. An aperiodic waveguide array is used to suppress the grating lobes of far-field beams, which enables a large FOV and small beam width. Meanwhile, to avoid crosstalk between antennas, a slab grating is used as the emitter. The experimentally demonstrated modulators have a half-wave voltage (V_π) of 6.42 V and a modulation bandwidth of 2.5 GHz. 2D beam scanning with a 50° × 8.6° FOV was realized by combining phase tuning and wavelength scanning. The beam width is 0.73° × 2.8° in the phase tuning direction (φ) and the wavelength scanning direction (θ), respectively.

2. DESIGN AND OPTIMIZATION

Figure 1(a) shows the schematic of the proposed high-speed OPA, which mainly consists of a four-stage cascaded multimode interference (MMI) splitter tree, traveling-wave modulator array, and aperiodic waveguide array combined with a slab grating antenna. As shown in the cross-sectional view of Fig. 1(b), the X-cut TFLN platform with a 600 nm thick lithium niobate (LN) layer and 2 μm buried oxide (BOX) layer is considered in our work. The device is covered with an 800 nm thick silica cladding. Considering the modulation efficiency of EO modulators and the complexity of fabrication, all waveguides and gratings have the same etching depth of 300 nm. The input laser is coupled to the chip through a grating coupler and then divided into 16 channels with the 1 × 16 MMI splitter tree. The modulator array provides independent phase control for each channel, and GS coplanar transmission lines are placed on both sides of the waveguide to drive the EO modulators. Figure 1(c) shows the TE_0 mode of the waveguide in the modulation region and the distribution of the static electrical field. The output of the modulators is fed into the same slab grating antenna for in-plane interference steering as well as out-of-plane radiation, as shown in Fig. 1(d).

The modulator array is the key component for realizing high-speed TFLN OPA. In order to utilize the strongest EO coefficient γ_{33} of the LN crystal, the waveguide in the modulation region is transmitted along the y direction of the crystal axis. The waveguide width w is 1 μm, and the electrode gap g is chosen to be 4 μm to maximize the modulation efficiency while ensuring the optical absorption loss of the metal electrodes is negligible (<0.0001 dB/cm). The calculated half-wave voltage length product ($V_\pi L$) is 6.69 V · cm, which is slightly larger than the typical value reported for TFLN modulators, mainly due to the upper cladding weakening the overlap of the electric and optical fields. The bandwidth of a traveling-wave modulator depends on the impedance matching, velocity matching between microwave and optical signals, and microwave losses [21]. The signal width and the ground width are optimally chosen as 40 μm and 100 μm, respectively. The electrode thickness h is 900 nm. Figure 2(a) shows the distribution of the microwave field at the radio frequency (RF) of 20 GHz.

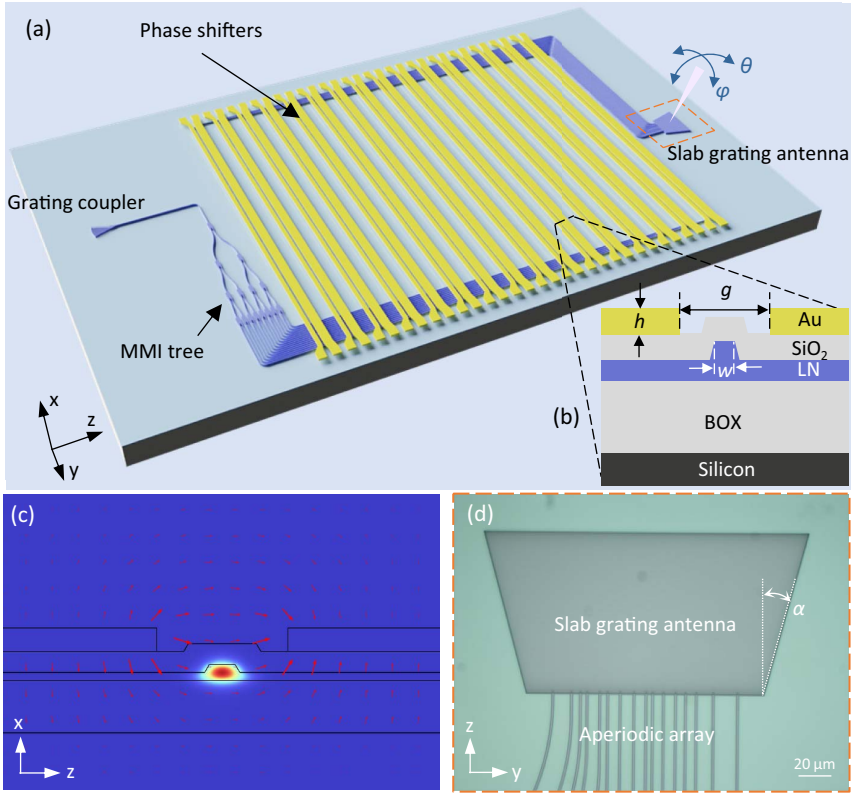

Fig. 1. (a) Schematic of the proposed TFLN OPA. (b) Cross-sectional view of the device. (c) Simulated optical mode field and static electrical field distribution in the modulation region. (d) Optical microscope image of the fabricated slab grating antenna.

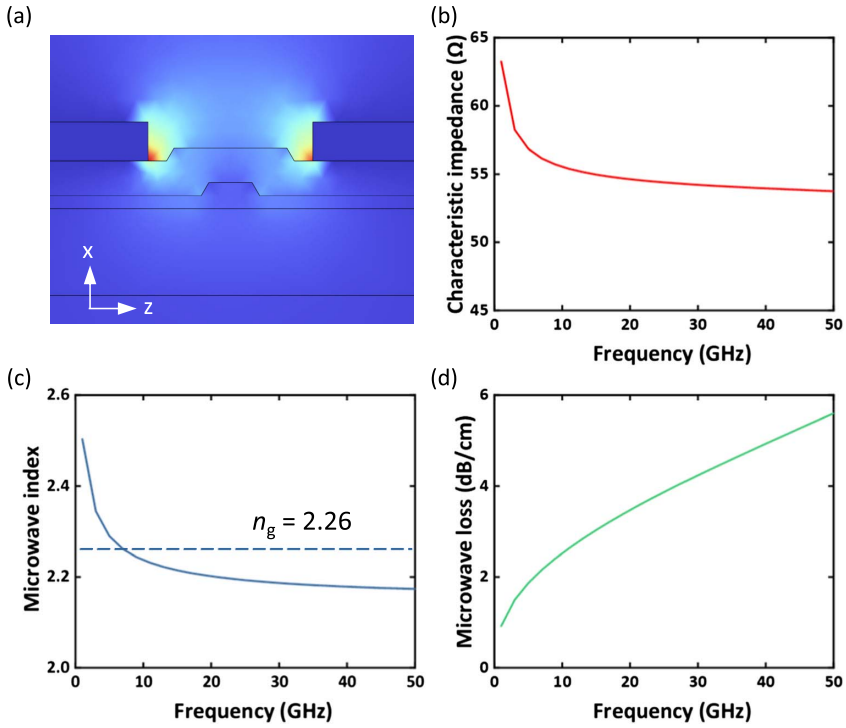

Fig. 2. (a) Simulated microwave mode profile. Calculated frequency dependence of (b) characteristic impedance, (c) microwave index, and (d) microwave loss.

The calculated results of the characteristic impedance, microwave index, and microwave loss with microwave frequency are shown in Figs. 2(b)–2(d). Here we choose the length of the modulation region L to be 1 cm, and the theoretical modulation bandwidth can be greater than 50 GHz.

Compared with a silicon waveguide, a TFLN waveguide has weaker optical field confinement as well as wider waveguide width, making it difficult to realize a dense waveguide array, which will lead to a limited FOV for TFLN OPAs. Here, we utilize an aperiodic array to suppress the grating lobes. A genetic algorithm is used to optimize the array element spacing over a range from 4 μm to 15 μm. Figure 3(a) shows the simulation results of the far-field distribution of the optimized aperiodic array. The whole aperture size of the waveguide array is 114 μm, which corresponds to a far-field beam width of 0.7°. As shown in Fig. 3(a), we find that the sidelobe suppression ratio (SLSR) is about 9–5.3 dB over a beam steering range of 50°. It should be noted that the relatively low SLSR is mainly limited by the scale of the array elements. For example, the SLSR of greater than 9 dB can be achieved over a beam steering range of 60° when the number of channels for OPA is increased to 64. A conventional waveguide grating antenna will conduct light along the shallowly etched slab layer to neighboring antenna elements, resulting in significant crosstalk. To solve this problem, we use only one slab grating antenna instead of an antenna array. When the waveguide mode propagates into

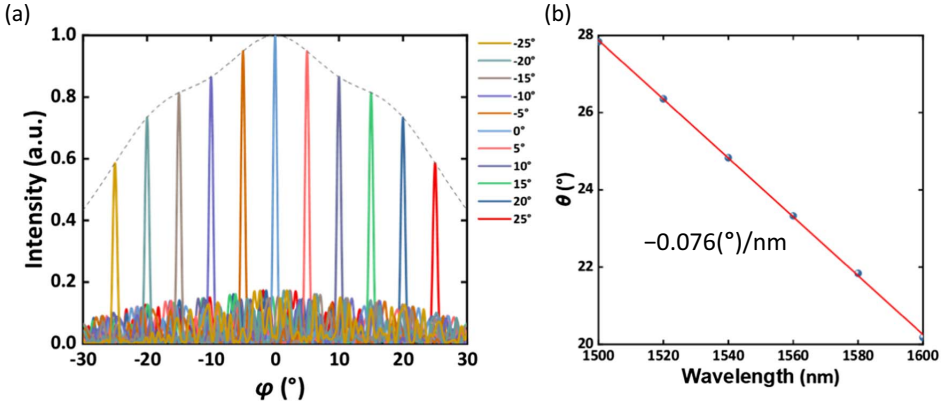

Fig. 3. (a) Calculated far-field distribution of the proposed OPA in the phase tuning direction. (b) Calculated steering angle varying with wavelength in the wavelength tuning direction.

the slab grating, it changes to a divergent slab mode for in-plane interference steering as well as out-of-plane radiation through the grating. The slab grating is designed as a trapezoidal shape, and the tilt angle is chosen to be 15°, which is larger than the in-plane divergence angle of the slab mode, so that more than 90% of the optical field power can be transmitted forward freely without being affected by the reflection of the sidewalls. Figure 3(b) shows the beam steering angle for different wavelengths, corresponding to a scanning efficiency of 0.076(°)/nm.

3. FABRICATION AND CHARACTERIZATION

The proposed TFLN OPA was patterned by electron-beam lithography (EBL), followed by the inductively coupled plasma reactive ion etching (ICP-RIE) process. Then 800 nm thick silica upper cladding layer was deposited using plasma enhanced chemical vapor deposition (PECVD). Finally, 900 nm thick coplanar waveguide electrodes were fabricated using a lift-off process. Figure 4(a) is the microscope image of the fabricated OPA chip, which includes the proposed OPA as well as a reference Mach–Zehnder interferometer (MZI) used to characterize the EO modulator. Figure 4(b) shows the image of the electrical and optical packaged chip. Pads for all modulators on the chip are bonded to the print circuit board (PCB) via gold wires and then connected to the voltage source and the load resistors (50 Ω). A fiber array was also packaged on the chip for optical characterization. By characterizing the losses of the unit components, we estimated that the total insertion loss of the OPA chip before the antenna emission is about 9.95 dB, which should be further optimized.

We measured the $V_\pi L$ and the bandwidth of the traveling-wave modulator first. As shown in Fig. 5(a), the lightwave of 1550 nm wavelength is coupled into the reference MZI after passing through the fiber polarization controller (FPC). A 10 kHz triangle signal generated by the arbitrary function generator (AFG) drives one of the two arms of the MZI. The modulated optical signal is detected by the oscilloscope (DSO) via a photodetector (PD). Figure 5(b) shows the variation of normalized output light intensity with driving voltage. It can be found that the $V_\pi L$ is 6.42 V · cm, which is in good

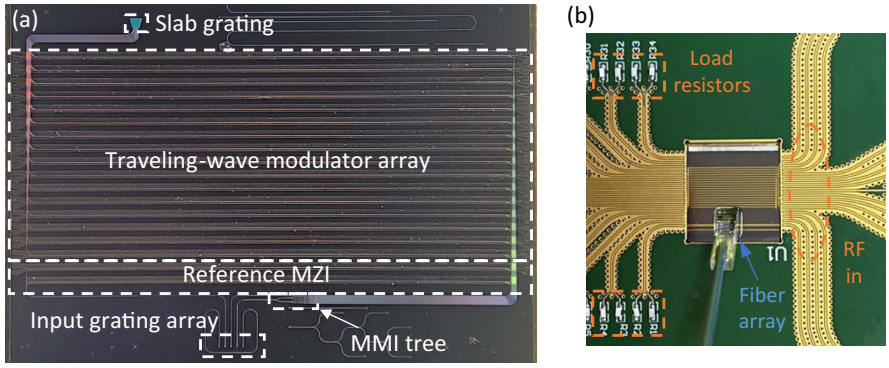

Fig. 4. (a) Optical microscope image of the fabricated chip. (b) Image of electrical and optical packaged chip.

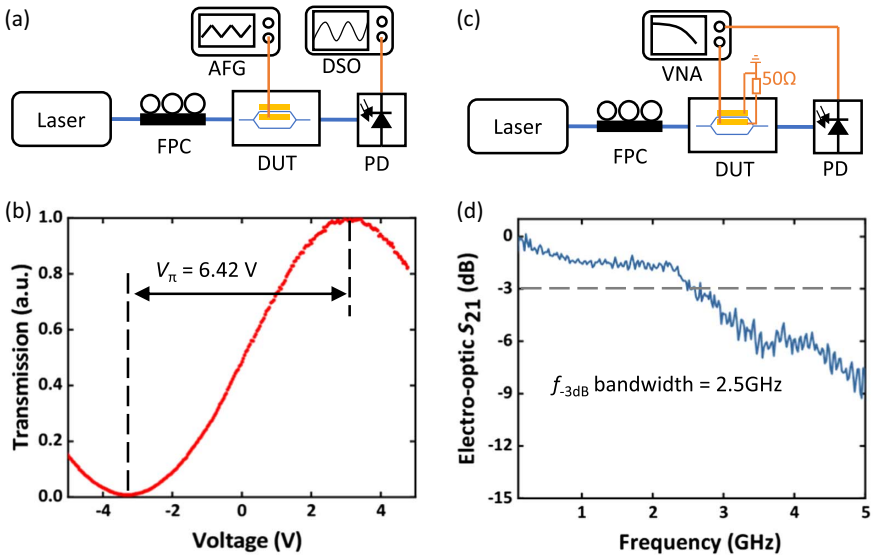

Fig. 5. (a) Schematic of the measurement setup for V_π. (b) Measured optical transmission response as a function of the applied voltage. (c) Schematic of the measurement setup for the small-signal EO response. (d) Measured EO S_{21} of the MZI modulator.

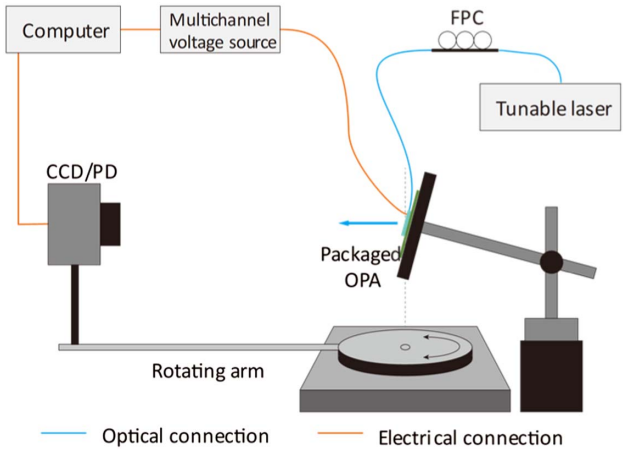

Fig. 6. Schematic diagram of the far-field characterization setup.

agreement with the simulation results. We also measured the small-signal EO S-parameters of the modulator using the vector network analyzer (VNA), as shown in Fig. 5(c). Figure 5(d) shows the measured EO response (S_{21}) of the MZI modulator, where the 3 dB modulation bandwidth is about 2.5 GHz. Such modulation bandwidth may be mainly limited by fabrication errors of the large-scale modulator array and the electrical packaging of the OPA chip. Therefore, in order to realize high-speed OPAs, an advanced fabrication process and electrical packaging techniques are also crucial. For a traveling-wave electrode modulator, the energy consumption is about $W_e = V_\pi^2/(f_{\mathrm{BW}} \cdot R)$, where f_{BW} is the operating bandwidth, and R is the load resistance [20]. When the device operates at 2.5 GHz, each modulator corresponds to a power consumption of 0.33 nJ/π.

Figure 6 is the schematic diagram of the far-field characterization setup. The packaged OPA is placed in the center of the rotating stage, and the stochastic parallel gradient descent (SPGD) algorithm is used to optimize the drive voltages for phase calibration. After calibrating the phase error, the PD on the rotating arm is replaced by a CCD camera, which is rotated to capture the far-field distribution over the entire FOV. It should be noted that we observe a degradation of the beam quality, when we continuously apply the optimized voltage. The direct current (DC) drift phenomenon is a common problem in LN modulators, which is caused by several mechanisms, including thermo-optic effect, pyroelectric effect, photorefractive effect, electrical relaxation, and so on [26]. It is possible to suppress DC drift by removing the cladding of lithium niobate waveguides [27]. At the wavelength of 1550 nm, we measure the far-field distribution when the beam is steering in the φ direction, as shown in Fig. 7(a). The optical intensity distribution at different steering angles is shown in Fig. 7(b). We can see that the SLSR is greater than 5.1 dB in the whole 50° FOV, which is basically consistent with the simulation results. As mentioned in previous analysis, the SLSR can be significantly improved by increasing the array element scale. The array number is mainly limited by the footprint of the lithium niobate-on-insulator (LNOI) modulator, which could be further optimized by looping the optical path in the modulation region [28]. By tuning the wavelength, the beam can be steered in the θ direction. As shown in Figs. 7(c) and 7(d), we realize a beam steering range of 8.6° by changing the wavelength from 1500 nm to 1620 nm, which corresponds to a scanning

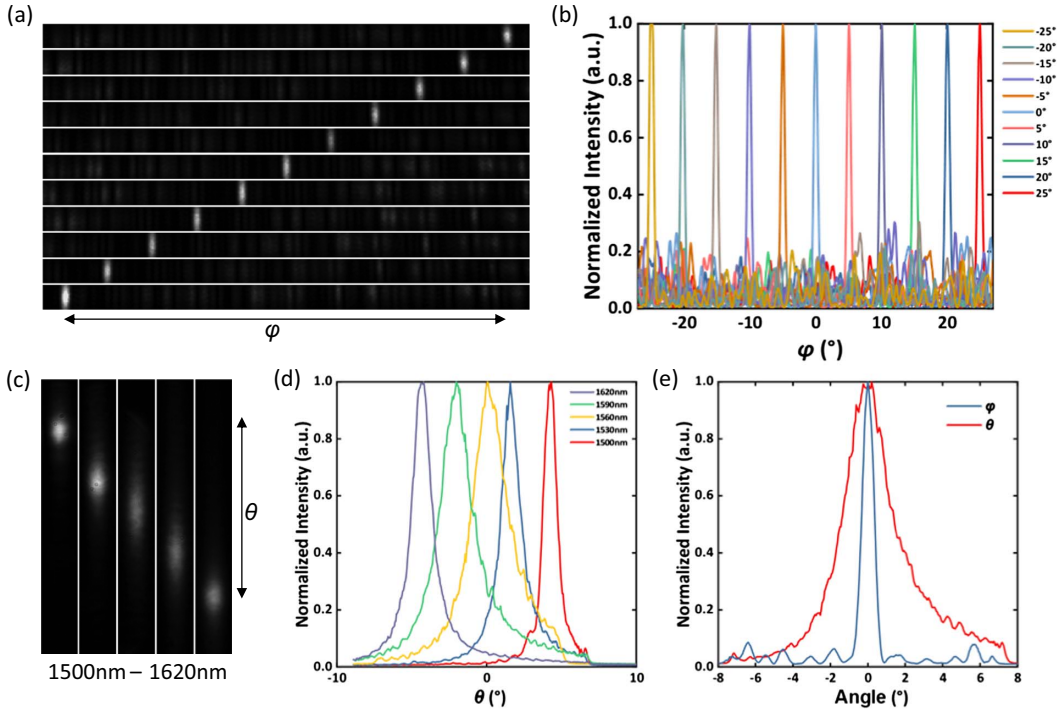

Fig. 7. (a) Image of far-field distribution and (b) measured optical power distribution versus angle in the phase tuning direction. (c) Image of far-field distribution and (d) measured optical power distribution versus angle in the wavelength scanning direction. (e) Measured beam width.

Table 1. Performance Comparison of the Reported High-Speed OPAs

Ref.	Platform	Modulation Mechanism	FOV (°)	Beam Width (°)	Power Consumption	Bandwidth
[14]	Si	Charge-injection	8.9 × 2.2	0.92 × 0.32	17 mW/π	324 MHz
[15]	EO polymer	Pockels effect	19.1	3.9	47.5 μW/π	2 MHz
[17]	InP	Carrier injection	8.88	0.11	48 mW/2π	<16 ns
[13]	Si	Carrier depletion	36 × 3.4	0.85 × 0.25	0.45 nW/π	700 MHz
[23]	TFLN	Pockels effect	24 × 8	2 × 0.6	13.5 pJ/π^a	4.2 GHz^a
This work	TFLN	Pockels effect	50 × 8.6	0.73 × 2.8	0.33 nJ/π	2.5 GHz

^{a}Simulation result.

efficiency of 0.07(°)/nm. Figure 7(e) shows the intensity distribution of the beam in the θ and φ directions at the wavelength of 1550 nm and the steering angle of 0°. The measured beam widths are 0.73° × 2.8° in the θ and φ directions, respectively. The beam width in the wavelength scanning direction (θ) can be improved by using a shallower etching depth grating [10] or by adopting a cladding grating design [29]. Table 1 compares the high-speed OPAs that have been reported on different platforms. It can be seen that our proposed OPA has a superior performance of modulation bandwidth and FOV.

4. CONCLUSION

In conclusion, we propose and demonstrate a 16-channel high-speed (GHz) TFLN OPA without grating lobes, for the first time, to the best of our knowledge. By using traveling-wave modulators and an optimized aperiodic array design, we experimentally achieve a modulation bandwidth of 2.5 GHz, an FOV of 50° × 8.6°, and a beam width of 0.73° × 2.8° in the phase tuning direction and the wavelength scanning direction, respectively. In the future, we will further increase the scale of the array elements and utilize grating antennas of weak radiation strength to improve the performance of SLSR as well as the beam width. In addition, antennas with wide radiation envelopes, such as chain grating antennas, and antennas with metasurface lenses, can be used to further enlarge the FOV [6,30]. We believe that such device will find its applications in high-speed holographic projection, free-space optical switching, and so on.

Funding. National Key Research and Development Program of China (2021YFB2801703); National Natural Science Foundation of China (62105286, 62135011); "Pioneer" and "Leading Goose" RD Program of Zhejiang (2022C01103); Natural Science Foundation of Ningbo Municipality (2023J282); Fundamental Research Funds for the Central Universities.

Disclosures. The authors declare no conflicts of interest.

Data Availability. Data underlying the results presented in this paper are not publicly available at this time but may be obtained from the authors upon reasonable request.

REFERENCES

1. S. Lin, Y. Chen, and Z. J. Wong, "High-performance optical beam steering with nanophotonics," Nanophotonics **11**, 2617–2638 (2022).
2. S. Zhao, J. Chen, and Y. Shi, "All-solid-state beam steering via integrated optical phased array technology," Micromachines **13**, 894 (2022).
3. C. V. Poulton, M. J. Byrd, P. Russo, B. Moss, O. Shatrovoy, M. Khandaker, and M. R. Watts, "Coherent LiDAR with an 8,192-element optical phased array and driving laser," IEEE J. Sel. Top. Quantum Electron. **28**, 6100508 (2022).
4. M. Raval, A. Yaacobi, and M. R. Watts, "Integrated visible light phased array system for autostereoscopic image projection," Opt. Lett. **43**, 3678–3681 (2018).
5. Y. Li, B. Chen, Q. Na, M. Tao, X. Liu, Z. Zhi, T. Peng, X. Li, X. Luo, G.-Q. Lo, F. Gao, X. Li, Q. Xie, and J. Song, "High-data-rate and wide-steering-range optical wireless communication via nonuniform-space optical phased array," J. Lightwave Technol. **41**, 4933–4940 (2023).
6. Y. Li, B. Chen, Q. Na, Q. Xie, M. Tao, L. Zhang, Z. Zhi, Y. Li, X. Liu, X. Luo, G. Lo, F. Gao, X. Li, and J. Song, "Wide-steering-angle high-resolution optical phased array," Photon. Res. **9**, 2511–2518 (2021).
7. P. Lu, W. Xu, C. Zhu, C. Liu, L. Lu, L. Zhou, and J. Chen, "Integrated multi-beam optical phased array based on a 4 × 4 Butler matrix," Opt. Lett. **46**, 1566–1569 (2021).
8. T. Fukui, R. Tanomura, K. Komatsu, D. Yamashita, S. Takahashi, Y. Nakano, and T. Tanemura, "Non-redundant optical phased array," Optica **8**, 1350–1358 (2021).
9. W. Li, J. Chen, D. Liang, D. Dai, and Y. Shi, "Silicon optical phased array with calibration-free phase shifters," Opt. Express **30**, 44029–44038 (2022).
10. Y. Liu and H. Hu, "Silicon optical phased array with a 180-degree field of view for 2D optical beam steering," Optica **9**, 903–907 (2022).
11. D. Liang, W. Li, X. Wang, X. Zhao, Z. Guo, X. Han, J. Chen, D. Dai, and Y. Shi, "Grating lobe-free silicon optical phased array with periodically bending modulation of dense antennas," Opt. Express **31**, 11423–11430 (2023).
12. W. Xu, Y. Guo, X. Li, C. Liu, L. Lu, J. Chen, and L. Zhou, "Fully integrated solid-state LiDAR transmitter on a multi-layer silicon-nitride-on-silicon photonic platform," J. Lightwave Technol. **41**, 832–840 (2023).
13. Z. Zhang, H. Yu, Q. Huang, Z. Zhou, B. Chen, T. Dai, H. Qiu, Y. Wang, and J. Yang, "High-speed and low-power silicon optical phased array based on the carrier-depletion mechanism," IEEE Photon. Technol. Lett. **34**, 271–274 (2022).
14. H. Zhang, Z. Zhang, J. Lv, C. Peng, and W. Hu, "Fast beam steering enabled by a chip-scale optical phased array with 8 × 8 elements," Opt. Commun. **461**, 125267 (2020).
15. Y. Hirano, Y. Miyamoto, M. Miura, Y. Motoyama, K. Machida, T. Yamada, A. Otomo, and H. Kikuchi, "High-speed optical-beam scanning by an optical phased array using electro-optic polymer waveguides," IEEE Photon. J. **12**, 6600807 (2020).
16. M. Gagino, M. B. J. van Rijn, E. A. J. M. Bente, M. K. Smit, and V. Dolores-Calzadilla, "Broadband operation of an InP optical phased array," IEEE Photon. Technol. Lett. **34**, 541–544 (2022).
17. K. Komatsu, Y. Kohno, Y. Nakano, and T. Tanemura, "Large-scale monolithic InP-based optical phased array," IEEE Photon. Technol. Lett. **33**, 1123–1126 (2021).
18. J. Midkiff, K. M. Yoo, J.-D. Shin, H. Dalir, M. Teimourpour, and R. T. Chen, "Optical phased array beam steering in the mid-infrared on an InP-based platform," Optica **7**, 1544–1547 (2020).

19. D. Zhu, L. Shao, M. Yu, R. Cheng, B. Desiatov, C. J. Xin, Y. Hu, J. Holzgrafe, S. Ghosh, A. Shams-Ansari, E. Puma, N. Sinclair, C. Reimer, M. Zhang, and M. Lončar, "Integrated photonics on thin-film lithium niobate," Adv. Opt. Photon. **13**, 242–352 (2021).
20. C. Wang, M. Zhang, X. Chen, M. Bertrand, A. Shams-Ansari, S. Chandrasekhar, P. Winzer, and M. Loncar, "Integrated lithium niobate electro-optic modulators operating at CMOS-compatible voltages," Nature **562**, 101–104 (2018).
21. Y. Zhang, L. Shao, J. Yang, Z. Chen, K. Zhang, K.-M. Shum, D. Zhu, C. H. Chan, M. Lončar, and C. Wang, "Systematic investigation of millimeter-wave optic modulation performance in thin-film lithium niobate," Photon. Res. **10**, 2380–2387 (2022).
22. G. Chen, K. Chen, R. Gan, Z. Ruan, Z. Wang, P. Huang, C. Lu, A. P. T. Lau, D. Dai, C. Guo, and L. Liu, "High performance thin-film lithium niobate modulator on a silicon substrate using periodic capacitively loaded traveling-wave electrode," APL Photon. **7**, 026103 (2022).
23. G. Yue and Y. Li, "Integrated lithium niobate optical phased array for two-dimensional beam steering," Opt. Lett. **48**, 3633–3636 (2023).
24. S. Tan, J. Liu, Y. Liu, H. Li, Q. Lu, and W. Guo, "Two-dimensional beam steering based on LNOI optical phased array," in *Conference on Lasers and Electro-Optics (CLEO)* (2020), paper SM2M.1.
25. Z. Wang, X. Li, J. Ji, Z. Sun, J. Sun, B. Fang, J. Lu, X. Chen, S. Zhu, and T. Li, "Fast-speed and low-power-consumption optical phased array," arXiv, arXiv:2304.11591 (2023).
26. J. P. Salvestrini, L. Guilbert, M. Fontana, M. Abarkan, and S. Gille, "Analysis and control of the DC drift in $LiNbO_3$ based Mach–Zehnder modulators," J. Lightwave Technol. **29**, 1522–1534 (2011).
27. Y. Xu, M. Shen, J. Lu, J. B. Surya, A. A. Sayem, and H. X. Tang, "Mitigating photorefractive effect in thin-film lithium niobate microring resonators," Opt. Express **29**, 5497–5504 (2021).
28. H. Huang, X. Han, A. Balčytis, A. Dubey, A. Boes, T. G. Nguyen, G. Ren, M. Tan, Y. Tian, and A. Mitchell, "Non-resonant recirculating light phase modulator," APL Photon. **7**, 106102 (2022).
29. Y. Wang, J. P. van Engelen, S. F. G. Reniers, M. B. J. van Rijn, X. Zhang, Z. Cao, V. Dolores-Calzadilla, K. A. Williams, M. K. Smit, and Y. Jiao, "InP-based grating antennas for high-resolution optical beam steering," IEEE J. Sel. Top. Quantum Electron. **27**, 6100107 (2021).
30. Z. Wang, W. Song, Y. Chen, B. Fang, J. Ji, H. Xin, S. Zhu, and T. Li, "Metasurface empowered lithium niobate optical phased array with an enlarged field of view," Photon. Res. **10**, B23–B29 (2022).